5th BSME International Conference on Thermal Engineering

Non-Linear Dynamics in Thermal and Reactive Fluid Flows

Toshihisa Ueda^a *

^a*Keio University, Department of Mechanical Engineering, 3-14-1, Hiyoshi, Kohoku-ku, Yokohama 223-8522, Japan*

Abstract

Fundamentals of non-linear dynamics in thermal and reactive fluid flows are presented with some recent topics. The concept of phase space, attractor, dimension, Poincare section will be summarized. The mixing and reaction in a high viscous fluid in an eccentric flow system of outer cylindrical vessel and inner cylindrical rod is discussed experimentally and numerically. The very slow alternative motion of the outer vessel and inner rod induces the chaotic motion with stretching and holding of fluid element without any turbulence and perturbations which enhances the mixing. The results show that there are two regions: one is a well-mixed region, that is a chaotic region, and the other is hardly mixed island region, that is a regular region. The experimental results of complex mixing and reaction patterns coincide well with numerical results not only qualitatively but quantitatively. This indicates that the complex phenomena observed is not a random one but the deterministic one even though the phenomena observed is very complex. The mixing in the static mixer, Kenics type static mixer, is discussed which shows the chaotic mixing in the steady state flow system by elements installed in the mixer. The results show that the elements with simple structure make stretching and holding effectively and then the mixing is enhanced extensively. The non-element mixing devices are discussed as well. The results show that the periodic flow variation makes the similar effect of the elements in the static mixer. A short term forward prediction is also demonstrated, using a Bunsen flame with burner rotation. When the burner is rotated, the flame tip starts to oscillate significantly because of the effect of the centrifugal force. When the rotating speed is increased, the oscillating motion becomes complex from a limit cycle to chaotic motion. The results demonstrated that the short term forward prediction can be done by using a concept of the chaotic dynamics. Through these interesting topics, I would like to emphasize the importance of non-linear dynamics, especially chaotic dynamics, in the thermal and reactive systems.

Nomenclature	
Y_i	mass fraction of species i
T	temperature (K)
U	jet velocity (m/s)
t	time (s)
v	velocity (m/s)
x, y, z	special coordinate
Δy_f	flame tip location
Greek symbols	
θ_i	rotational angle of inner rod
θ_o	rotational angle of outer cylinder

* Corresponding author. Tel.: +81-45-566-1496; fax: +81-45-566-1495.
E-mail address: ueda@mech.keio.ac.jp

1. Introduction

Mechanics of thermal and reactive flows is getting important in relation to Energy and Environmental issues. In many devices, such as engines, furnaces, chemical reactors, fuel cell, medical devices and so on, chemical reaction occurs with thermal, mass and momentum transfer and then the thermal and reactive fluid mechanics has been developed. Many good textbooks for transport phenomena (Bird et al. 2002) and, especially for reactive flows have been published (Law 2002, Williams 1985, Ueda 2002). In recent years, the dynamics for non-steady state motion has been developed because the many non-steady state issues have been left which are important from energy and environmental viewpoints. In some non-steady state phenomena, the motion changes non-linearly, which improve the efficiency dramatically but in some cases it induces serious accidents. Thus the non-linear dynamics is very important when we deal with non-steady state motion.

The non-linear dynamics has been developed from 1980's. This development showed new focus on many fields including thermal engineering. One of the important topics in the thermal engineering is the theory of dissipative structure. In the dissipative structure, a non-equilibrium state can make an ordered structure as a result of perturbation. In the fluid dynamics, the understanding of chaotic motion of fluid introduced a new concept between laminar flow and turbulent flow. The non-linear dynamics related to fluid flow motion, especially for mixing has been mentioned in the textbook written by Ottino (Ottino 1989)

In the present paper, then, I would like to explain the basic concept of the non-linear dynamics in Chapter 2 and discuss about some topics of thermal and reactive flows, mixing and reaction in an eccentric flow field, mixing in Kenics static mixer, mixing in a non-element mixer and short term forward prediction in Chapter 3. In chapter 4, I will summarize an importance of the non-linear dynamics in thermal and reactive fluid flow fields.

2. Basic Concept of Nonlinear Dynamics

2.1. Phase space, Phase space diagram

A phase space is defined as a space in which all possible states of a system are represented. For simple mechanical systems, the phase space usually consists of all possible values of position and momentum variables. A plot of position and momentum variables as a function of time is called a phase plot or phase diagram. Figure 1 shows a schematic of phase diagram of simple mechanical system, which consists of position x and velocity v. In thermal and reactive fluid flow systems, thermodynamic states, which consist of pressure, temperature, species concentration, are possible states in addition to position and momentum. Figure 2 shows a schematic of a phase diagram of reactive fluid flow system, which consists of velocity v, temperature T and mass fraction of i species Y_i.

2.2. Dynamical motion of thermal and reactive fluid flow systems

Variations in signals of dynamical motion of thermal and reactive fluid flow systems are shown in Figure 3(a). When the flow velocity is low and the characteristic length is small, in other words the Reynolds number is small, the thermal and reactive fluid flow systems are very stable and the motion is steady state mainly because the viscous effect plays a dominant role. All variables in a steady state motion are independent from time and the signal is flat with tine. When the flow velocity is increased and/or characteristic length is increased, the convective effect gradually plays significant, and the motion becomes unstable and starts to vary with time and the periodic motion is observed. The bifurcation of motion takes place and the bi-periodic motion is observed with further increase in the flow velocity and the characteristic length. With further increase in flow velocity and characteristic length, the successive bifurcation of motion occurs and the motion becomes complex gradually and becomes unpredictable complex motion. Here, the motion is a deterministic chaotic motion which means that the motion is a strictly deterministic time evolution, no matter how the motion is complicated. In other words, the motion can be traced and predicted. The motion finally becomes random which cannot be traced and then should be characterize by statistical methods with further increase in flow velocity and characteristic length.

2.3. Attractor

In order to characterize dynamical motion, the attractor is useful. The attractor is a phase space diagram that shows universal characteristics of the motion independent from initial conditions. Figure 3(b) shows the attractors corresponding to signals in Figure 3(a). For the steady state motion, no variation occurs and then the attractor becomes point, which is referred to "point attractor". For the periodic motion, the attractor becomes closed cycle, which is referred to "limit cycle". For the bi-periodic motion, the attractor becomes torus shape, which is referred to "torus attractor". For the chaotic motion,

the attractor shows some structure but not easily traced. The orbit does not come back to the previous one because the chaotic motion is not periodic. The attractor of chaotic motion is referred to "strange attractor". As for the random motion, the attractor becomes random as well and no characteristics can be seen.

2.4. Dimension

Dimension is one of the values of characterize the phase space diagram quantitatively. There are many ways to define the dimension in the non-linear dynamics. One of familiar dimensions is a capacity dimension. The capacity dimension is defined as,

$$dc = \lim_{\varepsilon \to 0} \frac{\log N(\varepsilon)}{\log(1/\varepsilon)} \qquad (1)$$

here, ε is the size of box to cover the figure and N is the number of box to cover the figure. The important point on the dimension in the non-linear dynamics is that the chaotic motion have non-integer dimension, and then the dimension of the strange attractor is non-integer.

2.5. Poincare section

A Poincare section is constructed by defining a surface of section in the phase space to simplify phase space diagram systematically. In other words, it is a stroboscopic view of the phase space diagram. Figure 3(c) shows the Poincare section corresponding to signals in Figure 3(a). As shown in limit cycle in Figure 3(b), the Poincare section is that of the cross sectional image of attractor. In fact, the cross sectional image of the limit cycle in Figure 3(b), that is the Poincare section, is a single point as shown in Figure 3(c) schematically when the direction of orbit is taken into account. It is interesting to note that the limit cycle reduces to point, torus to limit cycle, strange attractor to reduced strange attractor, random motion to reduced random motion.

2.6. Routes to Chaos

One of the interesting issues in thermal engineering is that how the phenomena become unstable. The non-linear dynamics addresses the variation of phenomena from stable to unstable condition as routes to chaos. In fact, the fluid flow becomes unstable and becomes turbulent with an increase in flow velocity. There are several routes. One is the period-doubling, which consists of a sequence of period-doubling bifurcations. The stable periodic orbit bifurcates and two orbits are cleated and bifurcate again into for orbits. After an infinite number of bifurcations, the system becomes chaotic. The other is the one shown in Figure 3. The stable state system, which is shown by a point attractor, turns to the limit cycle, the periodic oscillation. The limit cycle bifurcates to the torus attractor, which is characterized by two frequencies. The bifurcation occurs subsequently and finally turns into the strange attractor.
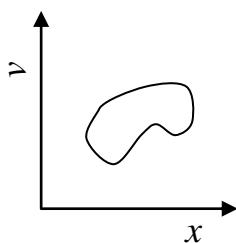
Figure 1 Phase Diagram
in Simple Mechanical Systems
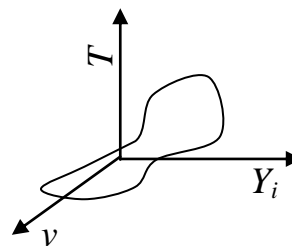(Position and Velocity)

Figure 2 Phase Diagram
in Reactive Fluid Flow Systems
(Velocity, Temperature and mass fraction of *i* species)

point attractor

Poincare section

limit cycle

torus attractor

strange attractor

random motion

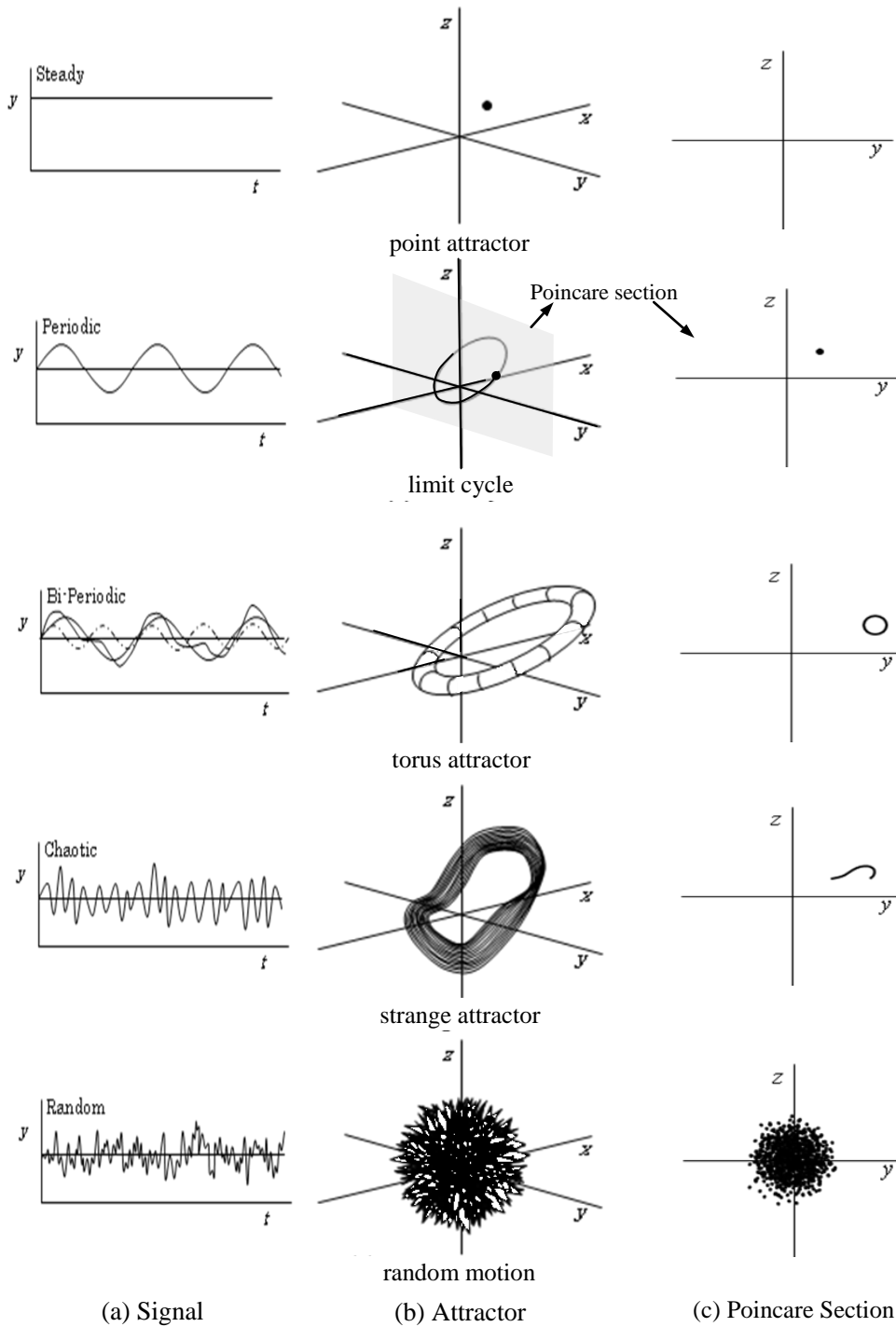(a) Signal   (b) Attractor   (c) Poincare Section

Figure 3 Signal, Attractor and Poincare Map

3. Non-linear Motion in Mixing and Reaction

3.1. Mixing and Reaction in an Eccentric flow (Sato and Ueda 2005)

One of the familiar chaotic mixing motions can be observed in an eccentric flow as shown in Figure 4(a). High viscous fluid, Glycerin, is set in an outer cylinder and two reactants are set in parallel each other. The outer cylinder and inner cylinder, which is set in an eccentric state, rotate alternatively in 180° with very low speed to remove instability from the fluid motion. Figure 4(b) shows the flow motion without chemical reaction. It is clearly seen that the stretching and folding occurs, which enlarges the fluid element. It is also interesting to note that the regular region where the significant stretching and folding cannot be seen is formed as well. Figure 4(c) shows the result with chemical reaction after 7, 10 and 20 alternative rotations. When the number of rotation is increased, the chemical reaction is enhanced. It is interesting to note that the chemical reaction takes place where the complex stretching and folding significantly takes place. In the regular region, on the other hand, the reactants are identified and no chemical reaction is observed.

The motion of the eccentric flow can be analyzed. The creep flow, in which no convective effect is considered, is assumed because the flow is induced by rotations of inner and outer cylinders and the fluid moved by the viscous effect. Figure 4(d) shows the bipolar coordinate used in the present analysis. The velocity at any location can be obtained analytically by using the bipolar coordinate. Each reactant is simulated by 10,000 particles shown at n=0 in Figure 4(e). Reactant Particles move with the velocity analyzed from the Lagrange viewpoint. Results after 7, 10 and 20 alternative rotations are shown in Figure 4(e). It is interesting to note that the numerical results show quite similar pattern with experimental one, which indicates that complicated mixing and reaction patterns can be traced.
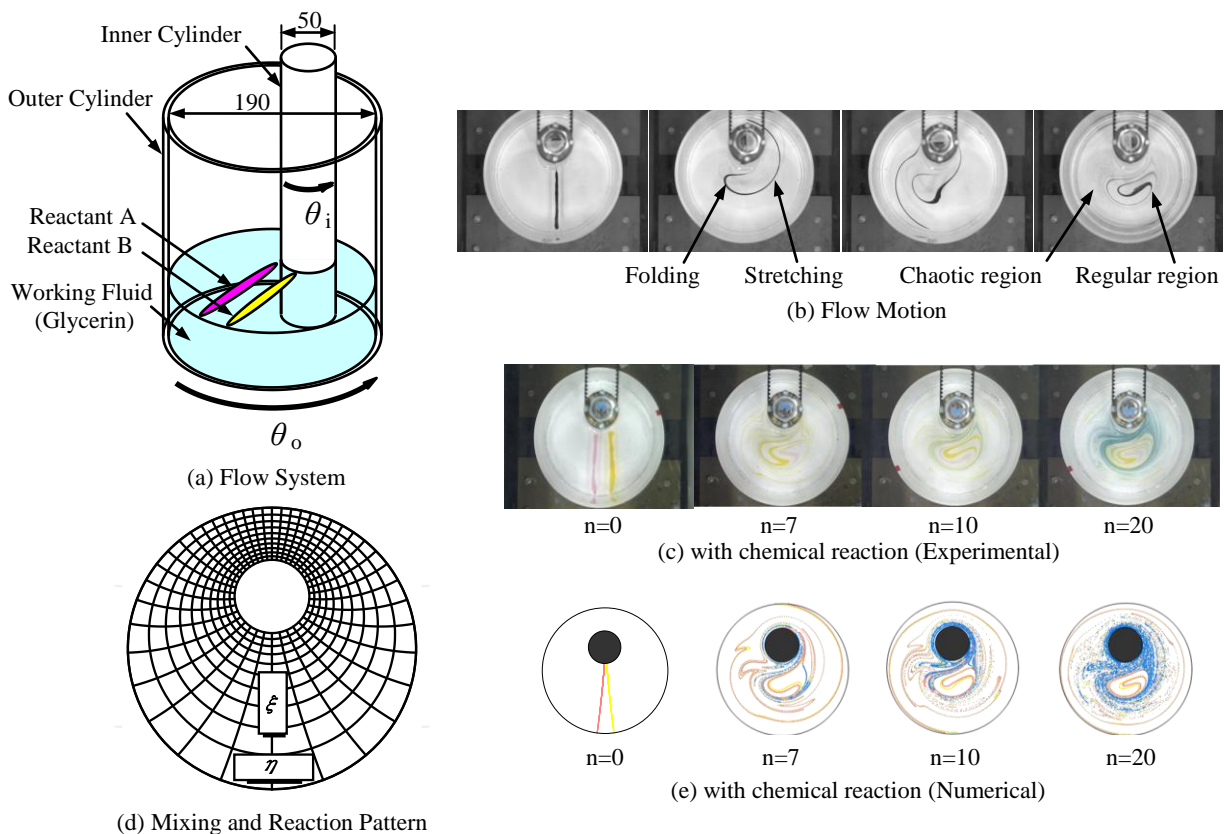

(a) Flow System

(b) Flow Motion

(d) Mixing and Reaction Pattern

(c) with chemical reaction (Experimental)

(e) with chemical reaction (Numerical)

Figure 4 Eccentric Flow Mixing and Reaction

3.2. Mixing in the Kenics Static Mixer (You et al. 2009-1)

Figure 5 shows the mixing in the Kenics static mixer, which is representative mixing device being applied chaotic mixing theory. Kenics static mixer is a continuous mixer shown in Figure 5(a) with element shown in Figure 5(b) inside. The mixing pattern is shown in Figure 5(c). Fluid is divided into two by each element and then the fluids is divided into small species in $2n$ through n elements. When the fluids pass 6 elements, fluids are divided into 64 small spices as shown in Figure 5(c), which enlarges the boundary of two fluids. Figure 5(c) also shows that numerical results well predict experimental ones.
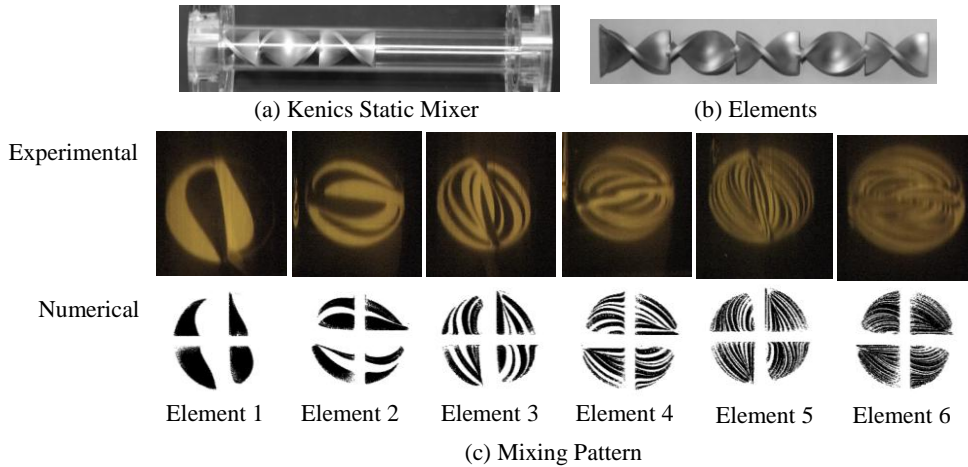

(a) Kenics Static Mixer   (b) Elements

(c) Mixing Pattern

Figure 5 Mixing of Kenics Static Mixer

3.3. Non-Element Mixer (You et al. 2009-2)

Non-element mixer is the continuous mixing device without elements inside developed by authors. As mentioned in Sections 3.1 and 3.2, simple periodic motion is necessary to make a flow chaotic. In the case of the eccentric flow, the simple periodic motion is realized by the alternative rotation of outer and inner cylinders. In the case of the Kenics static mixer, the simple periodic motion is realized by the elements. In the case of the non-element mixer, the simple periodic motion is realized by periodic injections of fluid from multiple side inlets. The mixing pattern is visualized by a Planer Laser Induced Fluorescence (PLIF) method. The fluorescent material is included in the side flow from inlet [1]. The stretching is significantly observed, especially in Figure 6(b) and the folding is seen in Figure 6(c) and 6(d). The boundary between two fluids enlarge which enhances the molecular level mixing.
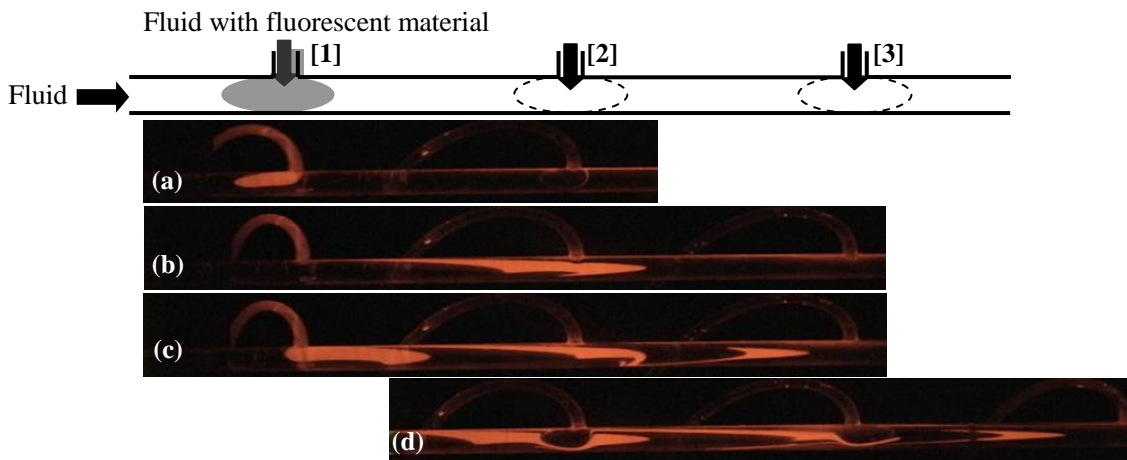

Figure 6 Mixing of Non-Element Mixer

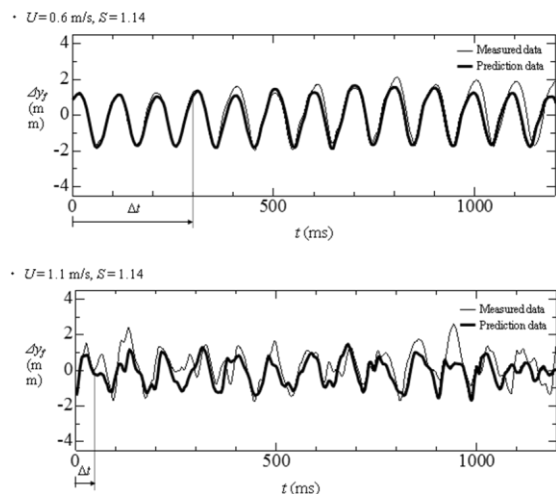*3.4. Short Term Forward Prediction (Gotoda and Ueda 2005)*

One of the important characteristics of non-linear dynamics is the possibility of short term forward prediction. Figure 7(a) shows the concept of the short term forward prediction. When we have a time series data of a motion, we can make an attractor. When we look into a local structure of the attractor, orbit lines are nearly parallel manner though lines don't coincide with each other. It means that we can consider the next motion will be similar to previous orbits. Thus, the short term forward prediction can be done. The experiments of the motion of the Bunsen flame tip have been done. The motion of the Bunsen flame tip varies as a function of the angular velocity of the premixed mixture. The experimental apparatus is shown in Figure 7(b). Figure 7(c) shows the comparison between the experimental results and the predicted results. When U=0.6m/s, the motion is periodic and then the predicted results fit very well with experimental results in 300ms. When U=1.1m/s, the predicted results fit with experimental results in about 50ms since the motion becomes complicated. This short term forward prediction for complicated motion will be useful to reduce serious accidents in chemical systems.
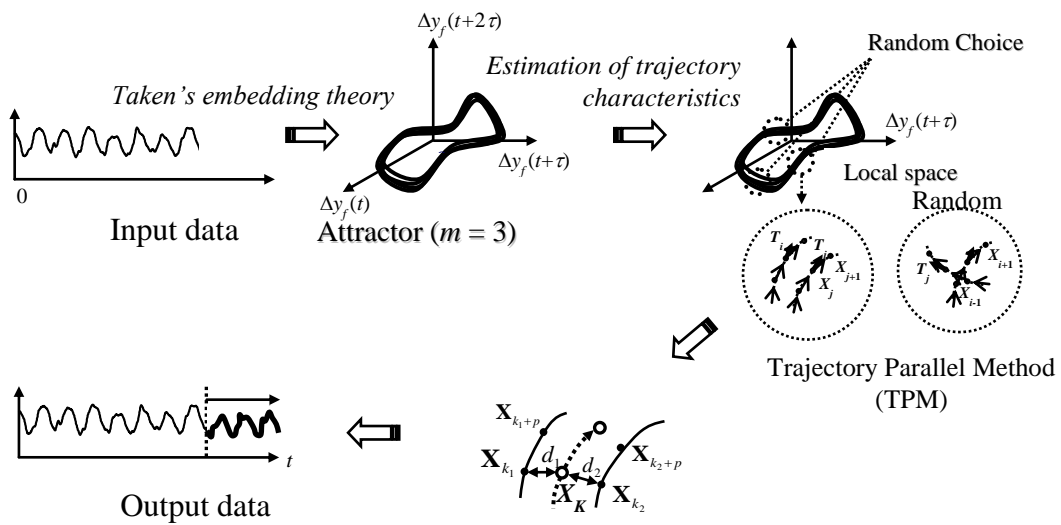
(a) Short term forward prediction method
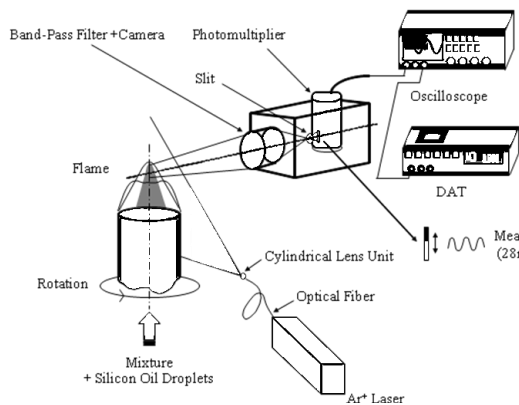
(b) Experimental apparatus

(c) Comparison between experimental result and predicted pattern

Figure 7 Short Term Forward Prediction

4. Summary

Fundamentals of non-linear dynamics of thermal and reactive fluid flows and some typical topics are presented to show potential to improve chemical systems. The chaotic motion enhances the mixing drastically, which results in a downsizing of the chemical and thermal systems. The chaotic concept makes possible the short term forward prediction which may reduce the serious accidents of chemical and thermal systems.

Acknowledgements

References

[1] Bird, R.B., Stewart, W.E. and Lightfoot, E.N., Transport Phenomena, Second Edition, John Wiley and Sons, New York, 2002.
[2] Law, C.K. Combustion Dynamics, Cambridge Press, 2006
[3] Williums, F.A., Combustion Theory, Second Edition, Benjamin/Cummings Publishing Company, 1985
[4] Ueda, T., Fluid Dynamics in Reactive Systems, Coronasha, 2002 (Japanese)
[5] Ottino,J.M, The Kinetics of Mixing: Stretching, Chaos, and Transport, Cambridge Texts in Applied Mathematics, Cambridge University Press, 1989,
[6] Sato,T. and Ueda,T., Mixing and reaction processes in high viscous fluids with alternate rotation of two eccentric cylinders, International Journal of Transport Phenomena, 7, pp.285-296, 2005
[7] You, S., Higuchi, N. and Ueda, T., Macroscopic estimation method of the mixedness of Kenics type static mixer, The Korean Journal of Chemical Engineering, 26, 6, pp.1497-1503, 2009
[8] You, S., Higuchi, N., Fujioka, S. and Ueda, T., Enhancement of Advective Mixing in a Non-Element Mixer, Kgaku Kogaku Ronbunshu, 35, 6, pp.589-595, 2009 (Japanese)
[9] Gotoda,H. and Ueda,T., Orbital Instability and Prediction of a Bunsen Flame Tip Motion with Burner Rotation, 140, pp.287-298, 2005

5th BSME International Conference on Thermal Engineering

Thermal oscillations and boiling flow oscillations in the natural circulation boiling loop

Arnab Karmakar, Nababithi Goswami, Swapan Paruya*

Department of Chemical Engineering, NIT Durgapur, India−713209

Abstract

Studies on thermal hydraulics in natural circulation boiling loop (NCBL) have wide applications in steam generators, boiling water reactors (BWRs), reboiler of a distillation column, chemical evaporators, etc. High heat transfer coefficient of the steam-water flow enables it to be useful as a primary cooling medium of the thermosyphon loops. The loop encounters several flow instabilities as reviewed in the recent past. Thus, temperature, pressure, flow rate and void fractions at the various parts of the loop oscillate. Oscillation of temperature in subcooled boiling, complex geometry of bubble-liquid interface, and instability in the boiling flow make the process more complex so that predictions and measurements of velocity, temperature, pressure and void fraction in the boiling channel become difficult and challenging. The heat transfer from the inner wall to bulk liquid in subcooled boiling is highly nonlinear phenomenon, and oscillation of heat transfer coefficient is coupled with the wall temperature oscillations.

The present experimental investigations report thermal oscillations and associated flow instabilities. The mechanism of thermal oscillations devised by Liu et al.[6] for forced-flow boiling has been extended to NCBL. Our experimental evidences support the mechanism with additional information. In the phase plane, out-of-phase oscillation of heat transfer coefficient with wall superheat is observed. At 4 kW heating rate and 50 ^{o}C inlet subcooling, the wall superheat varies in the range of 2-12 ^{o}C, whereas the heat transfer coefficients varies in the range of 6000-35000 W/m^2-K. At the lower inlet subcooling, the averages of wall superheat and heat transfer coefficient are higher compared to those at higher inlet subcooling, but vary in the narrower range. Power spectral densities of the loop flow rate were estimated by fast Fourier transform to find the fundamental frequency of oscillations and extent of chaos in the loop flow. Harmonics of primary frequency at higher inlet subcooling confirm the quasiperiodic to chaotic enroot as inlet subcooling is increased from 30 ☐ to 50°C.

Nomenclature

Q   heating rate(W)
ΔT_{sub} inlet subcooling(^{o}C)
ΔT_{sat} wall superheat(^{o}C)
Greek symbols
ψ   heat transfer coefficient(W/m^2-K)
Subscripts
sat   saturation
sub   subcooling

* Corresponding author. Tel.: +0-000-000-0000 ; fax: +0-000-000-0000 .
E-mail address: swapanparuya@gmail.com

1. Introduction

Natural circulation boiling loop (NCBL) containing steam−water mixture are used nowadays in evaporator, boiling water reactor and reboiler due to their excellent heat removal properties without the application of pump, compressor, etc. Various types of thermal hydraulic instabilities occur in a NCBL at the subcooled boiling condition and low pressure[1-3]. Under the subcooled boiling condition where steep temperature gradient exists in the narrow boiling channel, the interactions such as, wall−liquid, wall−bubble, bubble−bubble and bubble−liquid cause chaotic bubble growth and oscillations of temperature in the region. In the geysering instability presented in the literatures[4,5], vapor expulsion and its collapse due to condensation in subcooled liquid cause the flow stagnation and flow reversal. As a result of flow stagnation in the heated region, superheating of liquid occurs periodically associated with the geysering instability. Heater wall temperature oscillates periodically above a critical heating rate. The periodic oscillation of wall temperature with low frequency is known as thermal oscillation[3,6]. Extensive studies on the mechanism of thermal oscillations in NCBL are not available in literatures. Interaction of oscillating heat transfer coefficient with flow dynamics causes the thermal oscillation. Temperature oscillation in the heated solid (wall) in contact with a moving fluid occurs due to transitions between different boiling regimes (nucleate boiling, transition boiling, film boiling, etc.) of fluid. The temperature, pressure, loop flow rate at various sections of the loop oscillate vigorously with high amplitude and frequency in the boiling incipience of NCBL. The magnitude and characteristics of the oscillations depend on inlet subcooling ΔT_{sub}, heating rate Q and water content of the loop. In this work, the heat transfer characteristics of the boiling flow has been analyzed with experimental time series of the temperature, pressure and loop flow rate at boiling incipience of NCBL. The power spectrums of loop flow rate are also analyzed to characterize the oscillations and its contributing frequencies of different strength.

2. Experimental setup and procedure

The NCBL mainly consists of six parts — heated section, adiabatic riser, condenser, down-comer, and upper and lower plenum, respectively. The horizontally-oriented plenums (upper and lower plenums) connect the hot-leg and cold-leg of the loop. The rectangular loop-pipe was fabricated of SS 316. Different parts of the loop are manifolded to fit the temperature sensors and pressure sensors. Eight resistance temperature detectors (RTDs) (SS-310, 0−400 ^{o}C), are placed at various points of the loop. Three pressure (Gauge pressure, SS-310, 0−10 bar, WIKA Germany), are placed in the heater inlet and outlet and the end of the riser section. The loop pressure is controlled at the riser section. The electromagnetic flow meter (Electromagnetic, 20 mm polytetrafluoroethylene lining, 0−1.8 m^3/hr) is placed in the middle of the lower plenum section. The volumetric flow of water from downcomer is measured by the electromagnetic flow meter.

NCBL system also includes the cold-leg temperature controller (CLTC), pressure controller (PC), and heater-power controller (HPC). The data-logger software (DAQ) in the computer records data from all sensors in the system via supervisory control and data acquisition (SCADA) panel in the interval of 2-5 second. The distilled water as working fluid is heated at constant heater power and fixed pressure inside the loop. At the boiling incipience, the three fixed values of cold-leg temperature, i.e., 70 ^{o}C, 60 ^{o}C and 50 ^{o}C, correspond ΔT_{sub} of 30 ^{o}C, 40 ^{o}C and 50 ^{o}C were set in the cooling controller. In the conditions, data were recorded for 1-2 hour.

3. Result and discussion

In this section, the time series data of temperature, pressure and loop flow rate have been analyzed. The heat transfer coefficients are estimated with these time series at different Q and ΔT_{sub}. With the repetitive occurrence of wall superheating with geysering phenomena and complex interactions among wall, liquid and bubbles at the incipience of subcooled boiling flow, the oscillations of heat transfer coefficient occur. The wall temperature oscillations of low frequency (thermal oscillation) also take place. Fig. 1(a)-(b) show the thermal oscillations of outer wall temperature at the heater section at Q=4 kW and Q=5 kW. The frequency of the thermal oscillations increases with the increase in Q. There is no appreciable change of amplitude of thermal oscillations at two different Q. The high frequency slug bubbles generate in the heated section at high Q and low ΔT_{sub}, and boiling regime changes from nucleate boiling to transition boiling. Thermal oscillation occurs as the boiling heat transfer regime changes. In transition boiling regime, the wall temperature increases as the wall heat flux reduces. The wall temperature decreases as the boiling regime returns to the nucleate boiling. It occurs above a critical ΔT_{sub} and Q. With an increase in Q the high frequency slug bubbles quickly alter the boiling regimes, and the frequency of the thermal oscillation increases. The amplitude of the thermal oscillation depends on the relative magnitude of the extent of transition boiling and nucleate boiling.
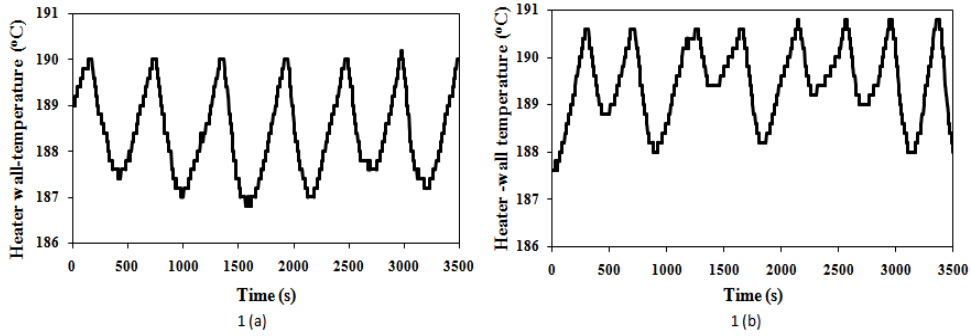
Fig. 1. Oscillations of outer wall temperature at the heater section at $\Delta T_{sub}=30\ ^{o}C$ (a) Q=4 kW and (b) Q=5 kW.

The fluid temperature at the heater outlet oscillates with the primary or dominant frequency and the secondary frequencies of lower strength. The primary frequency synchronizes with the frequency of the thermal oscillations, whereas the secondary frequencies are due to the geysering oscillations in the loop. Fig. 2 shows the oscillations of fluid temperature at the heater outlet at $\Delta T_{sub}=30\ ^{o}C$, and Q=4 kW and 5 kW. The frequency of primary oscillations increases with the increase in Q, as previously discussed thermal oscillations. The frequency and amplitude of secondary oscillations due to geysering decrease with the increase in Q.
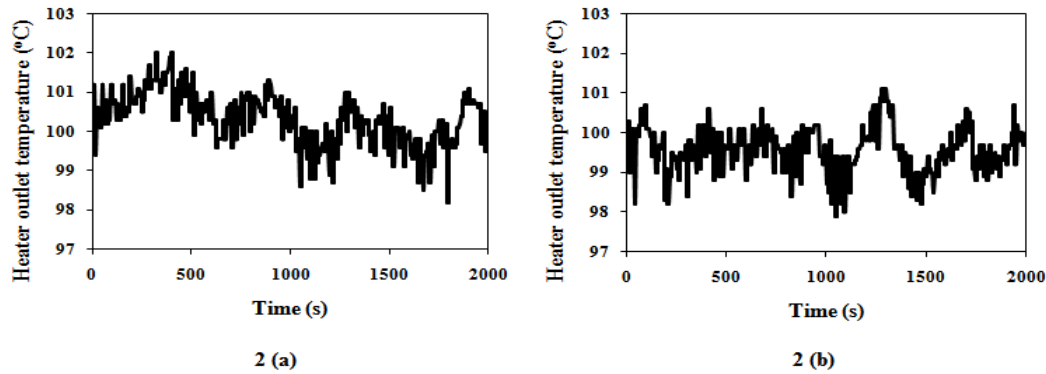

Fig. 2. Oscillations of fluid temperature at heater outlet at $\Delta T_{sub}=30\ ^{o}C$. (a) Q=4 kW and (b) Q=5 kW.

The Heat transfer mechanism in subcooled boiling is highly complex. The heat transfer from the heated wall to the bulk liquid has several components. A wide range of empirical models and mechanistic models have elegantly discussed by Warrier and Dhir[7]. The overall rate depends on the heat transfer rate from the wall to a bubble, wall to bulk liquid, bulk liquid to the bubble and bubble growth rate. This is very challenging to accurately predict the complex processes in the individual bubble−liquid−wall system, particularly in the situations of the chaotic and unstable flow in NCBL. In the present study, the heat transfer coefficient has been estimated and analyzed from experimental mass flow rate of the loop, temperature rise of the fluid being heated, heated wall temperature, and bulk liquid temperature. The rate of heat transfer from heated wall to bulk liquid depends on the heat transfer coefficient ψ being the function of the loop flow rate of fluid, fluid properties, wall surface geometry and thermal properties, and wall superheat ΔT_{sat}. For a given Q and ΔT_{sub}, the out-of-phase oscillations of ψ with ΔT_{sat} was observed, whereas the oscillations of ψ with loop flow rate are in-phase. Fig. 3 presents the phase portraits of ψ-ΔT_{sat} at different ΔT_{sub} at Q=4 kW. Two interesting things are noted. Both irregular oscillations (scattered points on the ψ-ΔT_{sat} space) and the out-of-phase oscillations are reduced as ΔT_{sub} is decreased, and two, the amplitudes of ψ-oscillations and ΔT_{sat}-oscillations significantly fall as ΔT_{sub} is decreased. At $\Delta T_{sub}=30^{o}C$, the drastic decrease of the amplitudes and more regular oscillations are the signature of the change of the heat transfer regime.

For a fixed Q and ΔT_{sub}, the heat transfer coefficients increase with increase in the loop flow rate which, in turn, causes the wall superheat to decrease. Peak value of heat transfer coefficient is observed when the high frequency bubble flow occurs in the heated section. If the wall superheat is not sufficient enough to initiate violent boiling, the loop flow rate does not increase significantly. In presence of fluid stagnation, the wall superheat starts to rise again. At Q=4 kW and ΔT_{sub} =50 °C, the wall superheat varies in the range of 2−12°C, whereas the heat transfer coefficient varies in the range of 6000−35000 W/m²-K. At Q=4 kW and ΔT_{sub}=40°C, ΔT_{sat} varies in the range of 5.22−12.22°C, whereas ψ varies in the range of 5400–24533 W/m²-K. At Q=4 kW and ΔT_{sub}=30 °C, ΔT_{sat} varies in the range of 7.8−13°C while ψ varies in the range of 6706–13970 W/m²-K. Thus, as ΔT_{sub} is increased, ΔT_{sat} and ψ oscillate with higher amplitude. At the lower ΔT_{sub}, the averages of ΔT_{sat} and heat transfer coefficient increase. It gives less chaotic instability in boiling flow at lower ΔT_{sub} compared to higher ΔT_{sub}. The oscillations of ψ and ΔT_{sat} are the main reasons for why the temperature of the fluid in contact with heated wall oscillates chaotically. The combined effect of unstable bubble dynamic and heat transfer dynamic, the various parameters in the NCBL oscillate.
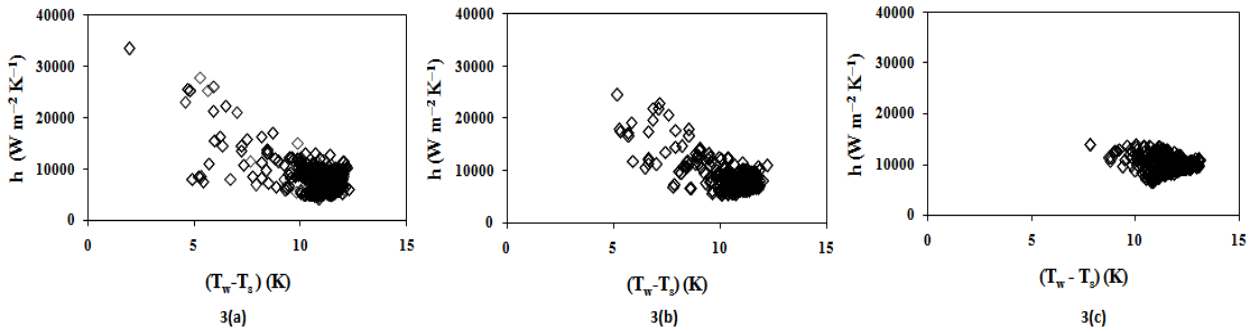

Fig. 3. The phase portrait of heat transfer coefficient with wall superheat at Q=4 kW and ΔT_{sub} of (a) 50 °C, (b) 40 °C, and (c) 30 °C.

The time series data taken during the experiments have been analyzed using power spectrums. The time series data of loop flow rates are converted to the frequency domain, and fast Fourier transform (FFT) has been carried out to estimate the power spectral density (PSD). Fig. 4 shows the PSD of the loop flow rate at Q=4 kW and different ΔT_{sub}. It has been noticed that the fundamental frequency increases with the decrease in ΔT_{sub}. At Q=4 kW and ΔT_{sub} of 50 °C, 40 °C and 30 °C, the respective fundamental frequencies are 0.0115, 0.029 and 0.0555 Hz. At Q=4kW and ΔT_{sub}=30 °C, high strength peaks at 0.0555 Hz correspond the quasiperiodic nature of flow oscillation. At the high ΔT_{sub}, the harmonics of the fundamental frequency correspond quasiperiodic enroute to chaotic flow oscillations. At Q=4 kW and ΔT_{sub}=50 °C, the harmonic frequencies are 0.0115, 0.0415 and 0.08 Hz. At the higher ΔT_{sub}, the flows are chaotic because of the wide distribution of bubble sizes and bubble frequencies. The same has been has been confirmed by direct visualization and high-speed camera.
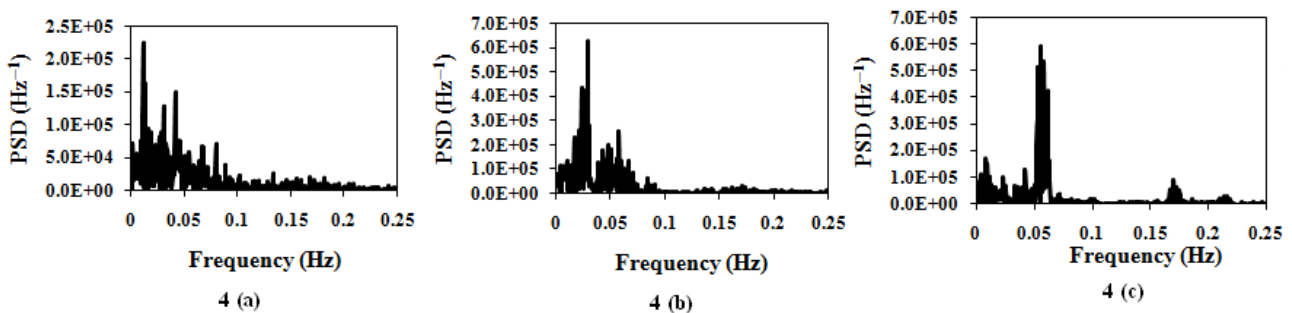

Fig. 4. The power spectral densities of loop flow rate at Q=4 kW and ΔT_{sub} of (a) 50 °C, (b) 40 °C, and (c) 30 °C.

Uncertainty analysis

While experimenting on boiling flow in a loop-pipe, there must be uncertainty with respect to instrument, measurement and overall process. In this study, the instrument uncertainties are negligible, as the uncertainties of all instruments including pressure sensors, RTDs and electromagnetic flow meter are less than 0.5 %. The standard deviations of loop flow rate for different sets of experiments at all conditions have been found to differ within $\pm 10\%$. This uncertainty comes from the controllability of CLTC. At different inlet subcooling, the fluctuations of cold leg temperature in CLTC are $\pm 2.5^{\circ}$C at ΔT_{sub}= 30 $^{\circ}$C, $\pm 2^{\circ}$C at ΔT_{sub}= 40 $^{\circ}$C, and ± 1.5 $^{\circ}$C at ΔT_{sub}= 50 $^{\circ}$C. It indicates that the controller performs better at high inlet subcooling. On the other hand, though the signals of loop flow rate are mostly homogeneous, a bit of nonstationary behavior is observed. For a pure homogeneous signal the standard deviation σ_n is independent of the length of time series n. On the other hand, depending upon nonstationary signal the σ_n depends on n, and the plot of σ_n vs. n grows with certain slope. Fig. 5 presents the plot of σ_n vs. n for loop flow rate at two different conditions. At Q=4 kW and ΔT_{sub}=40°C, loop flow rate signal is observed to be very close to stationary (slope = 0.007) while it slightly deviates from the stationary behavior (slope =0.018) at Q=5 kW and ΔT_{sub}=40°C.

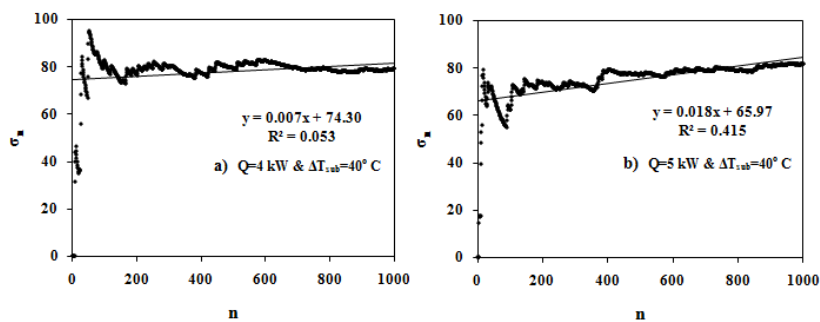Fig. 5. Plot of σ_n vs. n of loop flow rate at two different Q and ΔT_{sub}
(a) Q=4 kW & ΔT_{sub}=40° C (b) Q=5 kW & ΔT_{sub}=40° C

4. Conclusions

In the subcooled boiling of NCBL, the outer wall temperature in the heater section encounters oscillations above a critical inlet subcooling and heater power. The heater outlet temperature of fluid oscillates with secondary oscillation, whereas the primary oscillation of fluid temperature synchronizes with the thermal oscillations. The frequencies of thermal oscillation of wall temperature and primary oscillation of fluid temperature increase with the increase in heating rate. The amplitude and frequency of secondary oscillations increase with the increase in Q due to the generation high frequency slug bubbles. The out-of-phase oscillation of heat transfer coefficient with wall superheat was observed. With the increase in ΔT_{sub} the wall superheat and heat transfer coefficients of fluid in the heated section oscillate with higher amplitude. At the lower ΔT_{sub}, the wall superheat and heat transfer coefficient increase. Power spectrums of loop flow rate reveal that the oscillations of flow rate become more chaotic as ΔT_{sub} increases. The harmonics of the fundamental frequency in power spectrum were observed at high ΔT_{sub}, which are the indication of chaotic behavior of the oscillation of loop flow rate.

Acknowledgement

References

[1] Goswami, N., Paruya, S., 2011. Advances on the research on nonlinear phenomena in boiling natural circulation loop, Prog. Nucl. Energy 53, 673–697.
[2] Nayak, A.K., Vijayan, P.K., 2008. Flow Instabilities in Boiling Two-Phase Natural Circulation Systems: A Review, Science and Technology of Nuclear Installations 2008, 573192.
[3] Kakac, S., Bon, B., 2008. A Review of two-phase flow dynamic instabilities in tube boiling systems, Int. J. Heat Mass Transfer 51, 399–433.

[4] Paruya, S., Saha, A.K., Bhattacharya, P., 2009. Validations of thermohydraulic models for geysering in a natural circulation loop using an impedance needle probe, Ind. Eng. Chem. Res. 48, 2020−2033.

[5] Wu, C.Y., Wang, S.B., Pan, C., 1996. Chaotic Oscillations in a Low Pressure Two-Phase Natural Circulation Loop under Low Power and High Inlet Subcooling Conditions, Nucl. Eng. Des. 162, 223−232.

[6] Liu, H.T., Kakac, S., Mayinger, F., 1994. Characteristics of convective transition boiling and thermal oscillations, Int. J. Exp. Thermal Fluid Sci. 8, 195−205.

[7] Warrier, G.R., Dhir, V.K., 2006. Heat transfer and wall heat flux partitioning during subcooled flow nucleate boiling—a review, ASME Trans. J. Heat Transfer 128, 1243−1256.

5th BSME International Conference on Thermal Engineering

Prediction of Exterior Sound Pressure Field of a Cylinder Using the Boundary Element Method

Mir Md. Maruf Morshed*

Assistant Professor, Dept. of Mechanical and Chemical Engineering, Islamic University of Technology, Board Bazar, Gazipur-1704, Bangladesh

Abstract

The prediction of sound pressure field in the acoustic domain caused by a diffracting object is of interest in many fields of acoustics. Applications in acoustics include detecting, locating and classifying objects that generate a scattered sound field excited by the incident sound waves. For example, relevant to these applications; the exterior sound pressure field in the acoustic domain due to incident plane waves on a cylinder can be determined analytically and numerically. For the numerical investigation the Finite Element Method (FEM) is widely used. However, for the exterior acoustic problem the FEM requires discretization everywhere in the entire domain, which results in increase of computational time to solve the problem. In order to overcome this problem, the Boundary Element Method (BEM) has been used in the current work to construct a suitable numerical model. The analytical results confirmed the accuracy of the numerical results obtained using the BEM.

Nomenclature

E	Total number of surface elements
$H_m(z)$	Hankel function or Bessel function of the third kind of mth order and argument, z
$J_m(z)$	Bessel function of the first kind of mth order and argument, z
k	wavenumber
m	term number
$N_m(z)$	Neumann function or Bessel function of the second kind of mth order and argument, z
$p, \boldsymbol{p}$	nodal pressure; also, acoustic pressure, Pa
p^i	incident sound pressure, Pa
p^o	incident sound pressure amplitude, Pa
p^s	scattered sound pressure, Pa
p^t	total sound pressure, dB
X	X component of the cylindrical coordinate axes
Y	Y component of the cylindrical coordinate axes
ϕ	azimuthal angle, deg

---

* Tel.: +88 02 9291253-7 Ext. 3339; fax: +88 02 9291260.
E-mail address: marufm18@yahoo.com

1. Introduction

The sound pressure at locations in the acoustic domain surrounding the cylinder may generally be determined using the analytical expressions available in the literatures [1-5], due to incident plane waves that strike normal to the circumference of the cylinder. For the numerical analysis, Finite Element Method (FEM) and Boundary Element Method (BEM) can be used to determine the sound pressure at locations in the acoustic domain surrounding the cylinder. The use of BEM is based on the Helmholtz Integral Equation (HIE) and has been used in the past for the solution of interior and exterior acoustic radiation and scattering problems [6]. For problems related to the scattering from a rigid body, the integral equation can be modeled using the Neumann condition (the particle velocity normal to the boundary surface is zero) at the boundary [7]. Moreover, Sommerfeld's radiation condition of the radiating surface is automatically satisfied for the exterior infinite problem domain [8]. Basically, the integration relies on discrete boundary elements; hence the discretization is only needed on the boundary surface; in contrast, Finite Element Method (FEM) requires discretization everywhere in the entire domain of the problem [8]. Therefore, fewer nodes are required for meshing the boundary surface than needed for meshing the entire problem domain. This is one of the major advantages of BEM over FEM and it often results in less computational time to solve interior and exterior acoustic problems.

This work uses the BEM technique to predict the exterior sound pressure in the acoustic domain of the cylinder. The BEM software used here is written in MATLAB and is publicly available software known as Open BEM, which has been mainly developed by the Acoustic Laboratory, Technical University of Denmark. The numerical results using BEM are compared with the analytical results to ensure the validity of the numerical results. It should be noted that the determination of sound pressure at the surface of the cylinder has been extensively discussed in the literatures [9-11]; hence this study only focuses on the determination of sound pressure in the sound field not on the surface of the cylinder.

2. Theory

Consider plane waves travelling in the positive X direction and impinging normal to a cylinder of radius a as shown in Fig 1. In the figure, r is the radial distance from the origin of the cylinder, which can be any distance of interest from the cylinder. The directions $\Phi = 180°$ and $\Phi = 0°$ from the positive X axis will be considered as the front and back of the cylinder respectively. The governing equations for the incident, scattered and total pressure both on the surface and in the field can be written as follows [1]:

$$p^i(r,k,\phi) = p^o \sum_{m=0}^{M-1} \varepsilon_m i^m \cos(m\phi)\, J_m(kr)\,, \tag{1}$$

$$p^s(r,k,\phi) = -p^o \sum_{m=0}^{M-1} \varepsilon_m i^{m+1} e^{-i\gamma m} \sin\gamma_m \cos(m\phi)\, H_m(kr)\,, \tag{2}$$

$$p^t(r,k,\phi) = p^i(r,k,\phi) + p^s(r,k,\phi)$$

$$= p^o \sum_{m=0}^{M-1} \varepsilon_m i^m \cos(m\phi)\Big[J_m(kr) - i e^{-i\gamma m} \sin\gamma_m H_m(kr)\Big], \tag{3}$$

where the summation is for M number of terms required in the series calculations, $\varepsilon_m = 1$ if $m = 0$ and 2 if m > 0. The phase angles, γ_m, can be defined depending on the values of m as follows [2,4]:

$$\tan\gamma_0 = -J_1(ka)/N_1(ka) \qquad\qquad \text{when } m = 0$$

$$\tan\gamma_m = -J'_m(ka)/N'_m(ka) \qquad\qquad \text{when } m > 0. \tag{4}$$

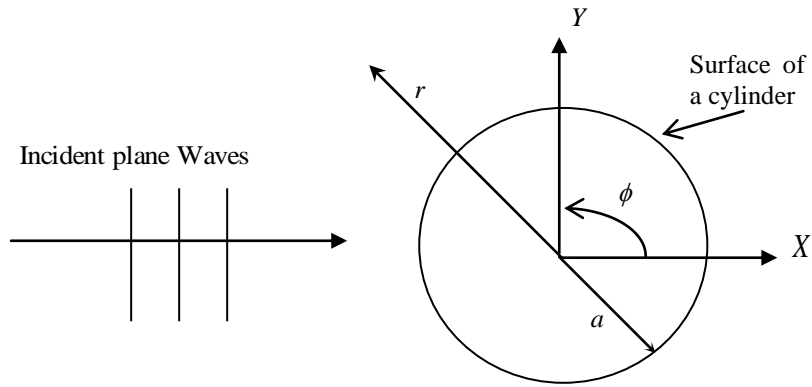Fig. 1. Incident plane waves traveling normal to the cylinder axis Z (Z axis is out of page).

3. Numerical Formulation

The determination of sound pressure in the sound field exterior to the boundary can be achieved using the Helmholtz integral equation, which can be written in the form

$$C(P)p(P) = \int_s p(Q) \frac{\partial}{\partial n} \left(\frac{e^{-ikR(Q,P)}}{R(Q,P)} \right) dS + p^i(P), \tag{5}$$

where Q and P are two points at some distance r_Q and r_P respectively, from the centre of the body as shown in Fig 2. In other words, one is the integration point on the boundary and the other is the field point which is placed outside the boundary. $R(Q,P) = |r_Q - r_P|$, $C(P)$ is the solid angle measured from the boundary and is equal to 2π for the two-dimensional exterior problem, $G(R) = e^{-ikR(Q,P)} / R(Q,P)$ is the free field Green's function and p^i represents the incident plane wave sound pressure on point P. Eq. (5) can be evaluated numerically by discretizing the boundary surface into E surface elements. The discretization of the integral Eq. (5) can be approximated by the sum of integrals over the elements as follows

$$C(P)p(P) = \sum_{i=1}^{E} \left[\int_{s_i} \left\{ p_i(Q)E_i(\xi) \frac{\partial}{\partial n} \left(\frac{e^{-ikR(Q,P)}}{R(Q,P)} \right) dS \right\} \right] + p^i(P), \tag{6}$$

where $E_i(\xi)$ are the element shape functions. For a surface formulation where $r_Q = r_P$, solving E calculations for all the elements on the surface, Eq. (6) can be written in the matrix form

$$[C]\{p\} = \{p\}[H] + p^i, \tag{7}$$

where $[C]$ is equal to $2\pi I_N$ (I_N is an $N \times N$ identity matrix of the N calculation points on the N nodes) for the surface formulation, and $[H]$ is an $H \times H$ global matrix of the H calculation points on the H elements. Here both $[C]$ and $[H]$ are known but the complex vector $\{p\}$ is unknown. Therefore to find $\{p\}$, Eq. (7) reduces to

$$[A]\{p\} = p^i, \tag{8}$$

where $[A] = [H - C]$. Equation (8), determines the total sound pressure only at the surface of the cylinder and needs to be extended for the sound pressure on the field points in the sound field. The matrix formulation for the total sound pressure on the field points becomes

$$\{p_f\} = [A_f]\{p\} - p^i_f, \tag{9}$$

where the subscript f denote the field points. $[A_f]$ is the coefficient matrix for the field points, p^i_f is the incident sound pressure on the field points and $\{p\}$ is the pressure associated with each node on the surface. $\{p\}$ can be calculated in a

similar way as indicated in equation (8) for the total pressure on the surface. On each surface and field node the incident sound pressure of equations (8) and (9) can be calculated for plane waves as follows:

$$p^i = p^i_f = p^o\, e^{i\,k\,x\,y} \quad , \tag{10}$$

where x and y represent the node position along the X and Y coordinates respectively. To calculate only the scattered sound pressure at the field points, the incident sound pressure term given in Eq. (9) can be omitted.
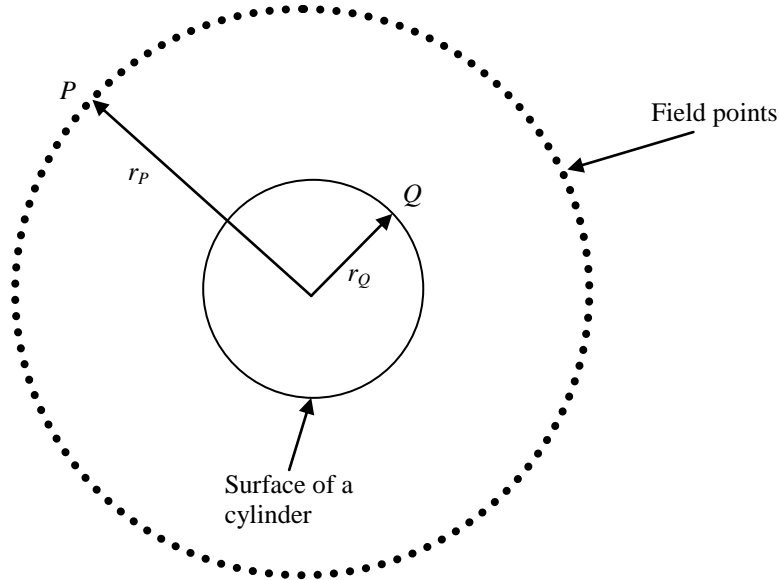

Fig. 2. Geometry of the exterior cylindrical problem.

4. Results and Discussions

The scattered and total sound pressures on each field point in the sound field (considering plane incident waves travelling from left to right) were calculated using Eq. (9) for the BEM analysis and compared with the analytical results calculated using Eqs. (2) and (3). The comparisons are shown between the analytical and BEM results for the scattered and total sound pressure distributions on the 80 field points placed circumferentially at a distance of $1.5a$ (one and half times the cylinder radius), $3a$ (three times the cylinder radius) and $5a$ (five times the cylinder radius) from the origin of a cylinder of radius a, for different values of ka in Figs (3-6) respectively. The results show very good agreement between the analytical and BEM techniques.

It can be seen in the Figs (3-4) that scattered pressure magnitudes decrease as the distance from the origin of the cylinder increases. This indicates that at a certain distance the scattered sound pressure will become zero and only the undisturbed incident sound pressure will remain. It is clear from the results that essentially there are no changes to the scattered sound pressure patterns around a cylinder in the sound field for a particular value of ka, but the scattered sound pressure patterns will be different for different wavelengths. On the other hand, it is noticeable from Figs (5-6), the total sound pressure pattern varies significantly with distance from the cylinder. For both the scattered and total pressure, there is more spatial variation in the sound pressure amplitudes when the wavelength is smaller than the circumference of the cylinder, as shown for the cases when $ka = 3$. The sound pressure is not uniformly distributed at the front of the cylinder, and a predominantly higher sound pressure is occurring at the back of the cylinder because of reinforcement of the two diffracted waves travelling around two sides of the cylinder. The computational time of the BEM calculations considering only 80 nodes is shown in Table 1 for a general computer (Intel (R) Core (TM) i5 dual-core, CPU 2.53GHz, RAM 4GB).

A large number of BEM calculations were also conducted to determine the scattered and total sound pressure fields around the cylinder. The calculations were made on 40,401 field points outside the cylinder for various values of ka. Numerical results are given for various values of ka in Figs 7 (a-d). The figures are a very good representation of the scattered and total pressure patterns for each value of ka around the cylinder. It can be seen that the scattered and total sound pressure are relatively smoothly varying, maximum at the front (left side of the figures) of the cylinder and varying more aggressively at the back (right side of the figures) of the cylinder. The reason has been discussed in the preceding paragraph and is a result of positive and/or negative interference of the two diffracted waves travelling around the two sides of the cylinder. Note that the scattered and total sound pressure patterns for each value of ka are similar to those presented in Figs (3-6).
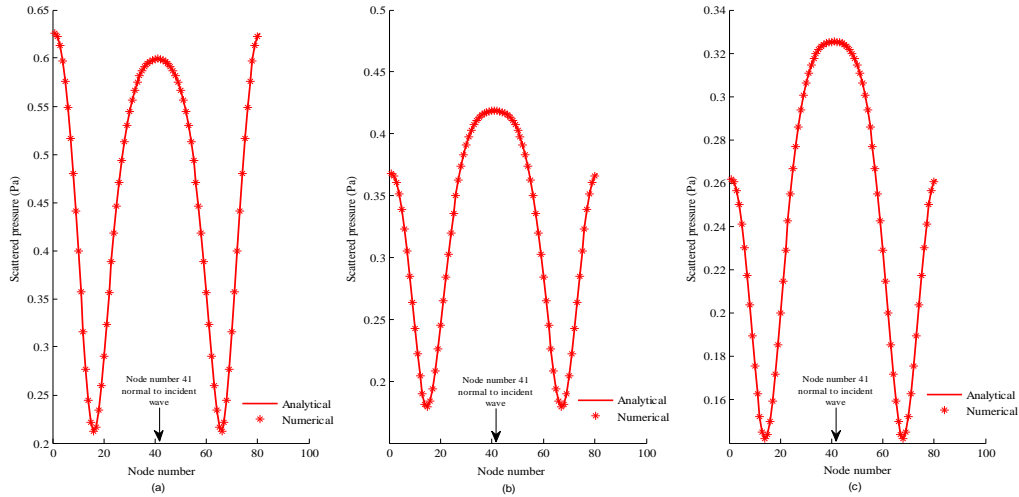
Fig. 3. Scattered sound pressure comparison between the analytical and numerical results at a distance of 1.5a, 3a and 5a, respectively, from the origin of a cylinder of radius a, for ka = 1. [Incident pressure amplitude p^o = 1 Pa]
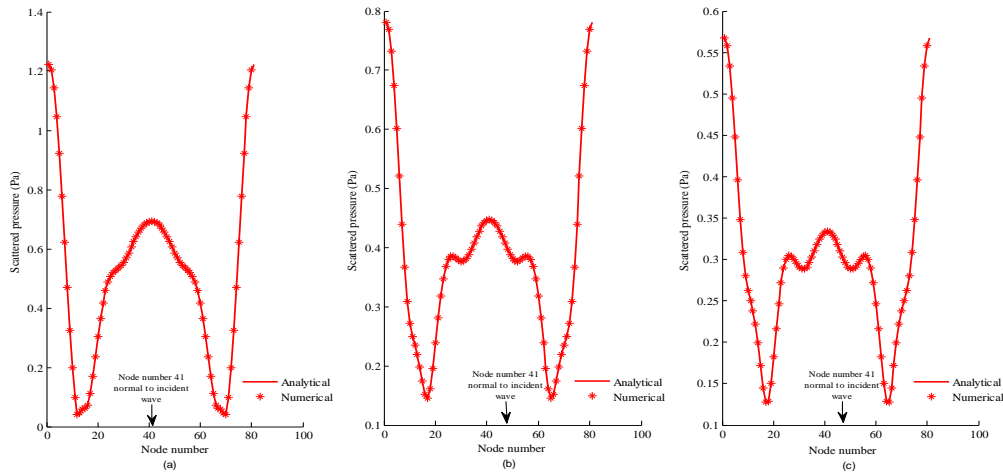

Fig. 4. Scattered sound pressure comparison between the analytical and numerical results at a distance of 1.5a, 3a and 5a, respectively, from the origin of a cylinder of radius a, for ka = 3. [Incident pressure amplitude p^o = 1 Pa]
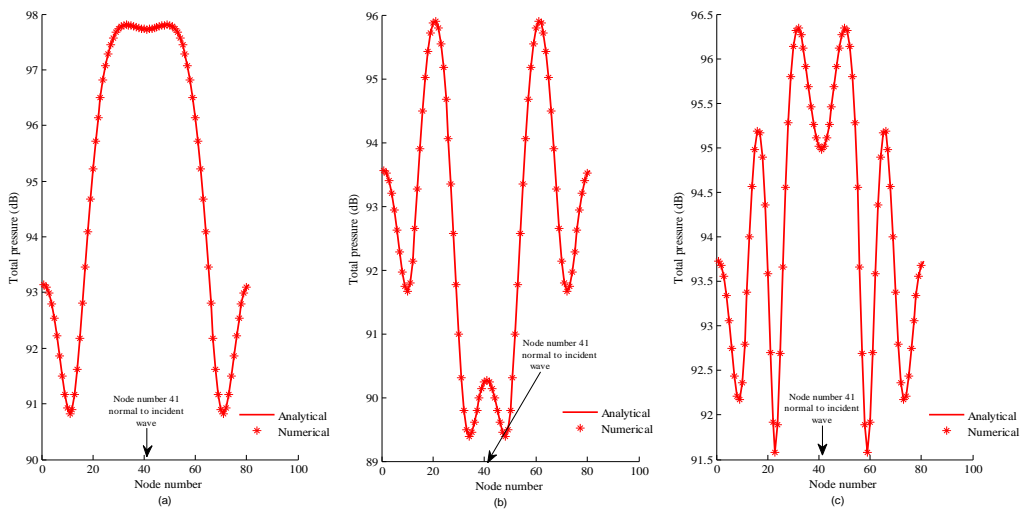

Fig. 5. Total sound pressure comparison between the analytical and numerical results at a distance of 1.5a, 3a and 5a, respectively, from the origin of a cylinder of radius a, for ka = 1. [Reference pressure 20μPa and incident pressure amplitude p^o = 1 Pa]
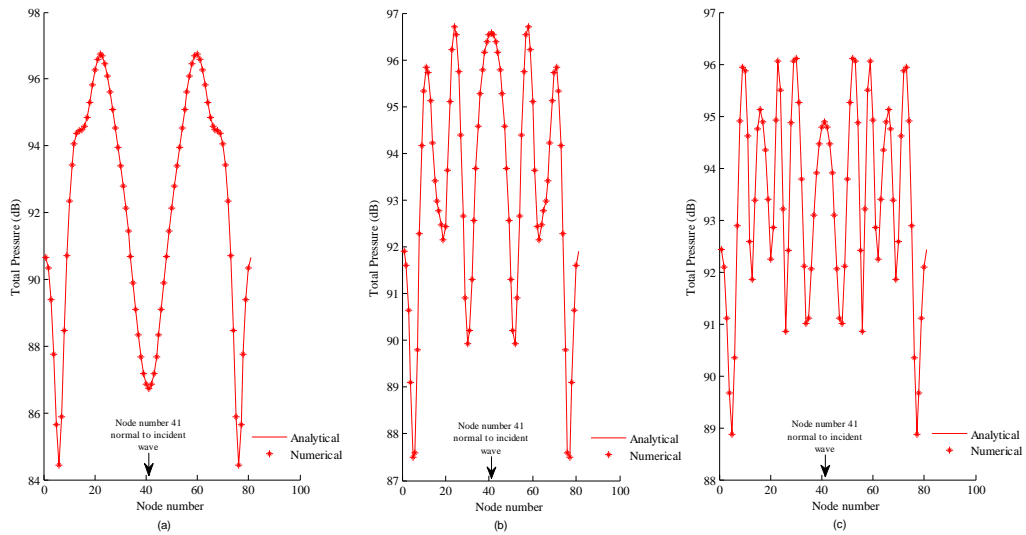
Fig. 6. Total sound pressure comparison between the analytical and numerical results at a distance of 1.5a, 3a and 5a, respectively, from the origin of a cylinder of radius a, for $ka = 3$. [Reference pressure 20μPa and incident pressure amplitude $p^o = 1$ Pa]

(a) Scattered pressure, $ka = 1$.

(b) Total pressure, $ka = 1$.

(c) Scattered pressure, $ka = 3$.

(d) Total pressure, $ka = 3$.
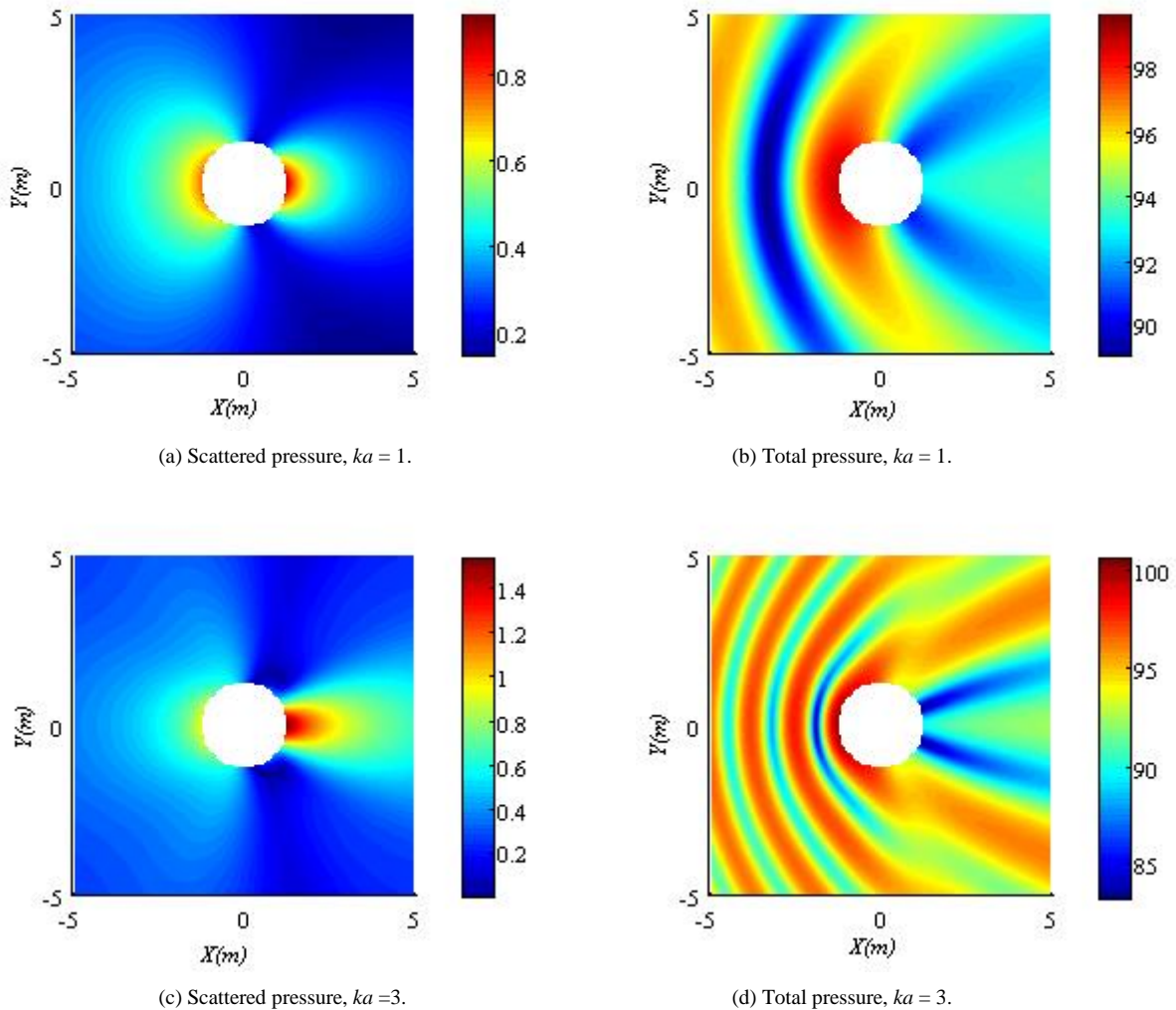
Fig. 7. BEM results showing the scattered and total sound pressure fields around a cylinder of radius a, for different values of ka. The scales for the scattered and total pressures are (Pa) and (dB) respectively. [Incident pressure magnitude $p^o = 1$ Pa and reference pressure 20μPa]

Table 1. Descriptions of numerical calculations

ka	Field point distance	Computational Time (sec)	Average computational time(sec)
	1.5*a*	4.9944	
1	3.5*a*	4.9449	
	5*a*	4.8786	
	1.5*a*	5.1888	5.0494
3	3.5*a*	4.6982	
	5*a*	5.5914	

5. Conclusions

It can be concluded from the comparisons between the results obtained using the analytical and Boundary Element Method (BEM) techniques that the BEM technique is suitable for calculating the sound pressure field at any location from a cylinder due to incident plane waves that strike normal to the circumference of the cylinder. It has been found from the results that predominantly higher sound pressure is occurring at the back of the cylinder because of reinforcement of the two diffracted waves travelling around two sides of the cylinder.

References

[1] Morshed, M. M. M., 2008. Investigation of External Acoustic Loadings on a Launch Vehicle Fairing During Lift-off. Ph.D. Dissertation, School of Mechanical Engineering, The University of Adelaide, SA, Australia.

[2] Morse, P. M., 1936. Vibration and Sound. 1st ed., McGraw-Hill Book Company, New York.

[3] Morse, P. M., Feshbach, H., 1953. Methods of Theoretical Physics Part-II. International student ed., McGraw-Hill Book Company, New York.

[4] Morse, P. M., Ingard, K. U., 1986. Theoretical Acoustics. McGraw-Hill Book Company, New York.

[5] Junger, C. M., Feit, D., 1993. Sound Structure and Their Interaction. MIT Press, New York

[6] Cunefare, K. A., Koopmann, G. A., 1989. Boundary Element Method for Acoustic Radiation Valid for all Wavenumbers, Journal of the Acoustical Society of America 85(1), p. 39-48.

[7] Kleinman, R. E., Roach, G. F., Schuetz, L. S., Shirron, J., 1988. An Iterative Solution to Acoustic Scattering by Rigid Objects, Journal of the Acoustical Society of America 84(1), p. 385-391.

[8] Hwang, J., Chang, S. A., 1991. Retracted Boundary Integral Equation for Exterior Acoustic Problem with Unique Solution for all Wave Numbers. Journal of the Acoustical Society of America 90(2), p. 1167-1180.

[9] Morshed, M. M. M., Zander, A. C., Hansen, C. H., 2010. "Sound Pressure at the Surface of a Cylinder Due to a Point Source," Proceedings of the 13th Asian Congress of Fluid Mechanics (13 ACFM). 17-21 Dec., Dhaka, Bangladesh, p. 212-215.

[10] Morshed, M. M. M., Zander, A. C., Hansen, C. H., 2011. Two-Dimensional and Three-Dimensional Acoustic Loadings on Cylinders Due to a Point Source, Journal of American Institute of Aeronautics and Astronautics (AIAA) 49(11), p. 2421-2429.

[11] Morshed, M. M. M., Hansen, C. H., Zander, A.C., 2011. "Sound Pressure Field Due to Obliquely Incident Waves on a Cylinder," Proceedings of the 18th International Congress of Sound and Vibration (ICSV18). 10-14 July, Rio De Janeiro, Brazil.